



Microstructure–property correlation and strain partitioning behavior in medium-carbon carbide-free bainitic steel

Ru Su¹ · Xiong-wei Zheng¹ · Jie Kang¹ · Da-yong Wu¹ · Hai-kun Ma¹ · Fu-cheng Zhang² · Zhi-nan Yang^{3,4} · Qing Li⁵

Received: 7 March 2024 / Revised: 27 April 2024 / Accepted: 15 May 2024
© China Iron and Steel Research Institute Group Co., Ltd. 2024

Abstract

The correlation between the microstructure, properties, and strain partitioning behavior in a medium-carbon carbide-free bainitic steel was investigated through a combination of experiments and representative volume element simulations. The results reveal that as the austempering temperature increases from low to intermediate, the optimal balance of properties shifts from strength–toughness to plasticity–toughness. The formation of fine bainitic ferrite plates and bainite sheaves under low austempering temperature (270 °C) enhances both strength and toughness. Conversely, the wide size and shape distribution of the retained austenite (RA) obtained through austempering at intermediate temperature (350 °C) contribute to increased work-hardening capacity, resulting in enhanced plasticity. The volume fraction of the ductile film-like RA plays a crucial role in enhancing impact toughness under relatively higher austempering temperatures. In the simulations of tensile deformation, the concentration of equivalent plastic strain predominantly manifests in the bainitic ferrite neighboring the martensite, whereas the equivalent plastic strain evenly spreads between the thin film-like retained austenite and bainitic ferrite. It is predicted that the cracks will occur at the interface between martensite and bainitic ferrite where the strain is concentrated, and eventually propagate along the strain failure zone.

Keywords Carbide-free bainitic steel · Strength · Retained austenite · Representative volume element · Strain partitioning

1 Introduction

Carbide-free bainitic steel, which is a preferred material for railway rails, bearings, and automotive components, is one of the best choices due to its low cost and excellent properties [1–3]. Nanosized or submicron bainitic ferrite plates, obtained through austempering or continuous cooling transformations, possess high density dislocations and provide high strength [4]. These plates are embedded with 10–25 vol.% soft retained austenite, which provides suitable plasticity and toughness [2, 5]. Consequently, research on the correlation between microstructures and characteristics obtained at various transformation temperatures can offer crucial direction for heat treatment procedures of bainitic steels.

In general, as the austempering temperature of bainite is decreased, the transformation driving force increases while the retained austenite (RA) volume fraction and bainitic ferrite plate size decrease; these effects eventually enhance steel strength. Bhadeshia and Edmonds [6] fabricated a high-carbon high-silicon nano-bainitic steel with ultrafine

✉ Jie Kang
ysdxkangjie@126.com

✉ Zhi-nan Yang
zhinanyang@ysu.edu.cn

¹ Hebei Key Laboratory of Material Near-Net Forming Technology, School of Materials Science and Engineering, Hebei University of Science and Technology, Shijiazhuang 050000, Hebei, China

² College of Metallurgy and Energy, North China University of Science and Technology, Tangshan 063210, Hebei, China

³ National Engineering Research Center for Equipment and Technology of Cold Strip Rolling, Yanshan University, Qinhuangdao 066004, Hebei, China

⁴ State Key Laboratory of Metastable Materials Science and Technology, Yanshan University, Qinhuangdao 066004, Hebei, China

⁵ Hebei Aerospace Superalloy Industry Technology Research Institute, Xingtai 054800, Hebei, China

bainitic ferrite plate and super high strength through austempering at 200 °C for an extended period. Cruz et al. [7] found that among medium-carbon high-silicon bainitic steel samples, the sample obtained through austempering at 220 °C has the best properties, which benefit from the presence of ultrafine bainitic ferrite plates and film-like retained austenite. The research conducted by Avishan et al. [8] suggests that the highest level of toughness is attained when the austempering temperature is set at 260 °C. Misra et al. [9] reported that the sample subjected to austempering at 350 °C has the best balance of strength and toughness. This characteristic is associated with the high amount and thermal stability of retained austenite and the high-carbon content of the retained austenite in austempering at intermediate temperatures [10–12]. Therefore, strength–plasticity or strength–toughness combinations can be controlled by the morphology and volume fraction of the phases present in the microstructure, which is determined by different austempering treatments.

The strength–plasticity performance of steel is controlled by the deformation and stress–strain partitioning behavior, which has been investigated through a combination of simulation and experimental approaches [13–18]. The advent of computational tools has revolutionized the study of deformation behavior by incorporating the actual microstructure [19–25]. However, conventional computational models like cellular automata (CA) [26], Monte Carlo (MC) [27], and Voronoi cell (VC) [28] may deviate from the actual microstructure and require extensive computational resources. In recent years, scientists have made strides in studying microscale mechanical behavior using a representative volume element (RVE) modeling approach. This method can resemble the real microstructure into the model and offers advantages surpassing other existing models. Moeini et al. [29] employed an RVE modeling approach based on dislocation density and Chaboche kinematic hardening to elucidate the tensile plastic deformation behavior of dual-phase steel. Vafaenezhad et al. [30] used RVE simulation to analyze the influence of the macroscopic mechanical properties of each phase in bainitic steel and effectively predicted its strength and plasticity.

In this work, various microstructure morphologies in medium-carbon high-silicon steel were obtained through austempering at different temperatures. The relationships between the microstructures and properties of the bainitic steel were investigated after tensile and impact testing. However, there is a non-monotonic relationship between microstructure and properties concerning the austempering temperatures, rather than a linear correlation reported in the literatures [6, 7]. It is considered that in the process of actual deformation, the large-sized blocky retained austenite (BRA) will transform into martensite at the initial

stage of deformation, while the film-like retained austenite (FRA) with high mechanical stability will not transform even under very high strain. Therefore, the microstructure basis of our RVE models is martensite–bainitic ferrite and film-like retained austenite–bainitic ferrite. The impact of different phases match on the stress–strain partitioning during tensile deformation of carbide-free bainitic steel is discussed.

2 Experimental material and process

The studied steel with the composition of C 0.46, Si 1.55, Mn 1.59, Cr 1.24, Ni 0.81, Mo 0.40, Al 0.62 and Fe balance (in wt.%) was produced by using a vacuum furnace and then forged into a round bar of $\phi 65$ mm. Samples were cut along the axial direction with dimensions of 25 mm \times 25 mm \times 115 mm. The transformation critical points for A_{c1} and A_{c3} of the test steel were measured using a dilatometer, with the tangent method yielding values of 753 and 795 °C, respectively, as shown in Fig. 1a. M_s transformation critical point was tested using a Gleeble 3500 thermal simulation machine, and the tangent method provided a value of 260 °C, as depicted in Fig. 1b. At the same time, the isothermal transformation curves (TTT curves) of the tested steel were also measured using a Gleeble 3500 thermal simulator in order to establish a reasonable isothermal bainite quenching process, as shown in Fig. 1c. The samples used in the Gleeble test are 10 mm in diameter and 10 mm in gauge. The test process is as follows: heating from room temperature to 600 °C at a rate of 10 °C/s, then to 930 °C at a rate of 1 °C/s, and finally austempering treatment at a rate of 30 °C/s to different temperatures.

Based on TTT curve of the tested steel (Fig. 1c), the heat treatment processes were performed as follows: the samples were austenitized at 930 °C for 45 min and then subjected to bainite transformation in a salt bath furnace. To contrast the performances of bainitic microstructures with varying morphologies, the austempering temperatures were selected as $M_s + 10$ °C (270 °C) to capture the typical lower bainite morphology and $M_s + 110$ °C (370 °C) to represent the typical upper bainite morphology. In addition, an austempering temperature of 350 °C was chosen based on the literature [1–3]. These works suggested that the microstructures subjected to austempering at 350 °C exhibited optimal strength and ductility properties. All of the samples underwent a 2 h austempering treatment. Finally, all of the samples were tempered at 320 °C for 1 h. In addition, the microstructure and properties of the sample subjected to oil quenching and tempering at 320 °C \times 1 h were also provided in Supplementary Materials.

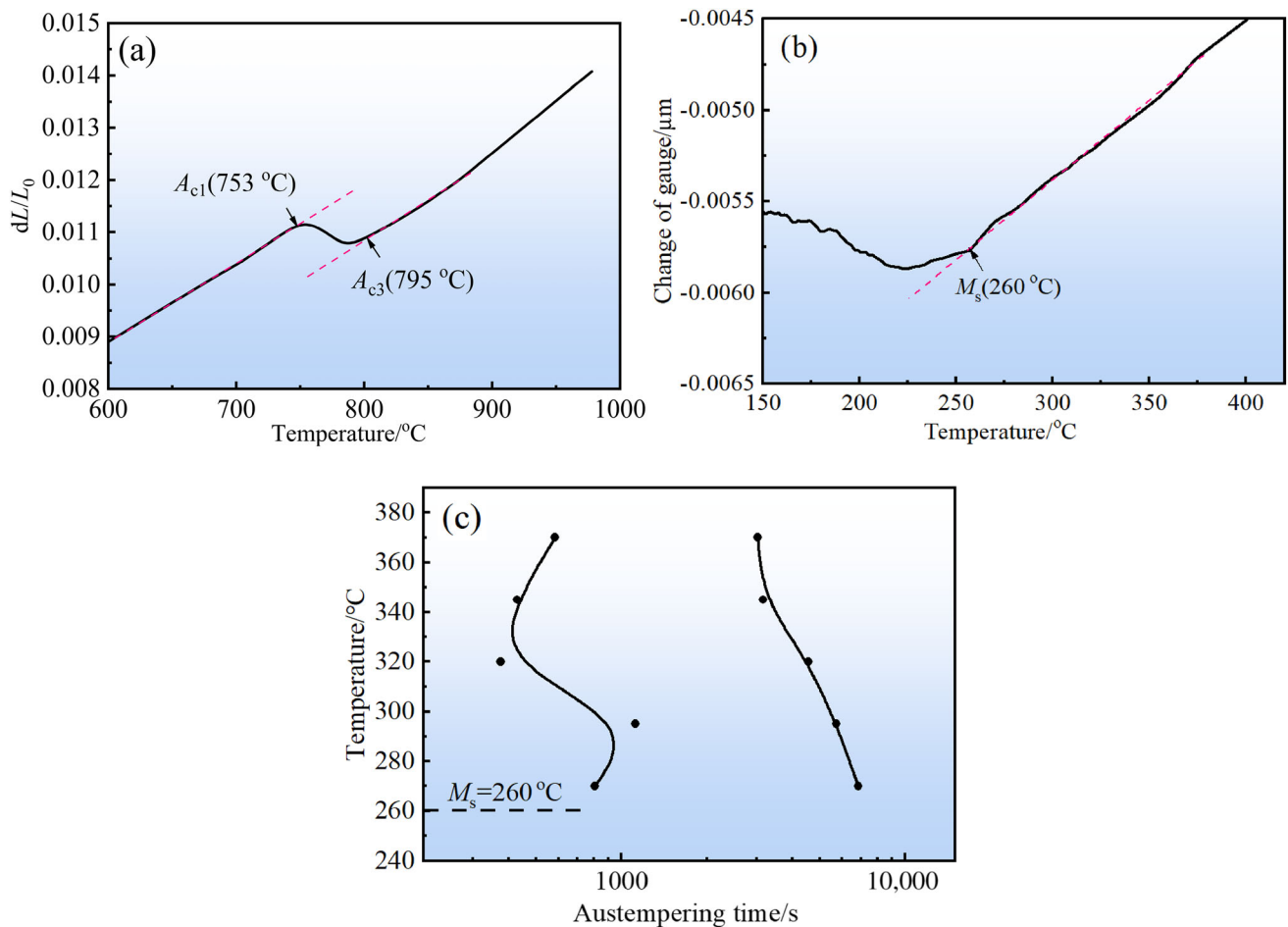


Fig. 1 Thermal expansion curves determining A_{c1} , A_{c3} (a) and M_s (b) and TTT curves (c) of studied steel

Tensile testing was performed on an MTS universal hydraulic testing machine with a strain rate of $4 \times 10^{-4} \text{ s}^{-1}$. The testing sample was a round bar with a gauge of 25 mm and a diameter of 5 mm. Impact testing was carried out using a pendulum testing machine on a sample with dimensions of 10 mm \times 10 mm \times 55 mm and a U-shaped notch.

Microstructures and substructures were observed and analyzed through scanning electron microscopy (SEM) and transmission electron microscopy (TEM). The sample used for TEM was prepared by utilizing a TenuPol-5 type twin-jet electropolishing instrument at room temperature. The electrolytic polishing fluid was 7 vol.% perchloric acid and 93 vol.% absolute ethanol solution. The operation voltage was 28 V. The morphology and misorientation of the bainite sheaf were observed and characterized through electron backscattered diffraction (EBSD). The sample was prepared using ion milling. During EBSD testing, the scanning step length of the instrument was set to 0.08 μm with an accelerating voltage of 60 kV. Phase components and relative volume fractions were tested using a Rigaku

D/max-2500/PC X-ray diffractometer (XRD) with a radiation target of Cu $K\alpha$ in step scanning mode with 0.2 ($^\circ$)/step. Each step lasted for 2 s. The volume fraction of the retained austenite (V_{RA}) is determined by Eq. (1) [31]. Carbon concentration in the retained austenite (C_{RA}) is determined by Eq. (2) [32] by using the lattice parameters of the retained austenite.

$$V_{\text{RA}} = \frac{(1/n) \sum_{j=1}^n I_{\gamma}^j / R_{\gamma}^j}{(1/n) \sum_{j=1}^n (I_{\gamma}^j / R_{\gamma}^j) + (1/n) \sum_{j=1}^n (I_{\alpha}^j / R_{\alpha}^j)} \quad (1)$$

$$a = 3.578 + 0.033C_{\text{RA}} \quad (2)$$

where n is the number of peaks examined; I is the integrated intensity of the diffraction peak; γ is the austenite and α is the ferrite; R is the material scattering factor, that is, $R = (1/v^2) \left[|F|^2 P ((1 + \cos^2 2\theta) / \sin \theta \sin 2\theta) \right] \cdot e^{-2M}$; v is the volume of the unit cell; F is the structure factor; P is the multiplicity factor; e^{-2M} is the temperature factor; θ is the diffraction angle; and a is the austenite lattice parameter.

3 Finite element model

In the microstructure of carbide-free bainitic steel, two distinct forms of retained austenite can be observed: blocky and film-like. The stability of RA is determined by several factors, including the carbon content, shape and size, as well as the conditions of the surrounding phase [33, 34]. The high-carbon content RA, in the form of a thin film, exhibits remarkable stability and is capable of maintaining its structural integrity even under high-strain conditions. This exceptional stability prevents any phase transformation from occurring, thereby significantly enhancing the work-hardening behavior of carbide-free bainitic steel. Consequently, the elongation of the steel is greatly improved [35]. However, RA with low carbon content and a blocky morphology exhibits relatively poor stability and is prone to transforming into martensite during the initial stages of deformation [36]. As a consequence, within the finite element simulation framework utilized in this research, we postulate that the blocky retained austenite undergoes a complete transformation into martensite during the initial stage of deformation. In contrast, the highly stable, film-like retained austenite does not convert into martensite until the ultimate tensile fracture occurs. Following this, a finite element analysis was carried out, based on this specific context.

The flow curves of each phase are defined using the strain hardening model based on the dislocation density theory [37, 38] as presented below:

$$\sigma = \sigma_0 + \Delta\sigma + \alpha f G \sqrt{b} \sqrt{\frac{1 - \exp(-fK\varepsilon)}{KL}} \quad (3)$$

where σ denotes the flow stress (von Mises stress); ε signifies the true strain; σ_0 represents the Peierls stress; $\Delta\sigma$ is the strengthening stress attributed to carbon by precipitation or solid solution; α represents a constant factor in this study, $\alpha = 0.33$ [39, 40]; f denotes the Taylor factor, $f = 3$; G signifies the shear modulus, $G = 80,000$; b represents the Burger's vector, $b = 2.5 \times 10^{-10}$; L denotes the average free path of dislocations; and K represents the recovery rate. The average dislocation free path in martensite is 3.8×10^{-10} m [37], while that in bainite is considered as the average distance between low-angle grain boundaries [41]. K of martensite is 41, while for bainite, K is considered to be $10^{-5}/d_\gamma$, where d_γ is the initial austenite grain size [42].

In Eq. (3), the initial term σ_0 signifies the Peierls stress, which relies on the chemical composition of distinct phases within the material and can be elucidated as:

$$\sigma_0 = 77 + 80m_{\text{Mn}} + 7500m_{\text{P}} + 80m_{\text{Cu}} + 60m_{\text{Si}} + 45m_{\text{Ni}} + 11m_{\text{Mo}} + 60m_{\text{Cr}} + 5000m_{\text{N}} \quad (4)$$

where m_i represents the mass fraction of alloying element i .

In Eq. (3), the second term $\Delta\sigma$ characterizes the enhanced stress induced by carbon through precipitation or solid solution. The contributions to this enhancement from the residual austenite ($\Delta\sigma_{\text{RA}}$), martensite ($\Delta\sigma_{\text{M}}$), and bainitic ferrite ($\Delta\sigma_{\text{BF}}$) are delineated as follows:

$$\Delta\sigma_{\text{RA}} = 5000m_{\text{C}_{\text{SS}}^{\text{R}}} \quad (5)$$

$$\Delta\sigma_{\text{M}} = 3065 - 161m_{\text{C}_{\text{SS}}^{\text{M}}} \quad (6)$$

$$\Delta\sigma_{\text{BF}} = 900m_{\text{C}_{\text{SS}}^{\text{B}}} \quad (7)$$

where $m_{\text{C}_{\text{SS}}^{\text{R}}}$, $m_{\text{C}_{\text{SS}}^{\text{M}}}$ and $m_{\text{C}_{\text{SS}}^{\text{B}}}$ represent the carbon content in the retained austenite, martensite, and bainitic ferrite phases, respectively.

4 Results

4.1 Microstructure characterization

Figure 2 shows SEM and TEM images of the microstructures in the studied steel after austempering at different temperatures. SEM observation reveals that the obtained microstructure is characterized by the presence of bainitic ferrite sheaves and film-like or blocky retained austenite. With the increase in austempering temperatures, the microstructure coarsens, and the ferrite/austenite phase boundary changes from flat to rough. TEM observation shows the presence of an FRA that is parallel to the bainitic ferrite plate or distributed at certain angles. In addition, BRA is present. In the sample subjected to austempering at 270 °C, most of the retained austenite is thin film-like in form and distributed within the bainitic ferrite (BF) at a certain angle. When the austempering temperature is decreased, this microstructure becomes film-like, and its size increases.

The phase fraction, morphology, size, and distribution of the bainitic ferrite and retained austenite can be summarized by combining the results of SEM, TEM, and XRD. The microstructure feature parameters are listed in Table 1. Information on V_{RA} and C_{RA} of the retained austenite, the fraction of blocky retained austenite (V_{BRA}), and the size of film-like retained austenite (t_{FRA}) can be obtained on the basis of the retained austenite. The bainitic ferrite plate width (t_{BF}) was divided by low-angle grain boundary (5° – 15°), and bainite sheaf size (L_{BF}) was divided by high-angle grain boundary ($> 15^\circ$). V_{RA} and C_{RA} were measured through XRD. V_{BRA} and L_{BF} were determined through SEM statistically. t_{BF} and t_{FRA} were determined through TEM statistically. The average linear intercept (\bar{L}_T^{BF}), which has a relationship with the actual thickness of the ferrite plate (t_{ab}), can be measured along the direction vertical to the bainitic ferrite plate.

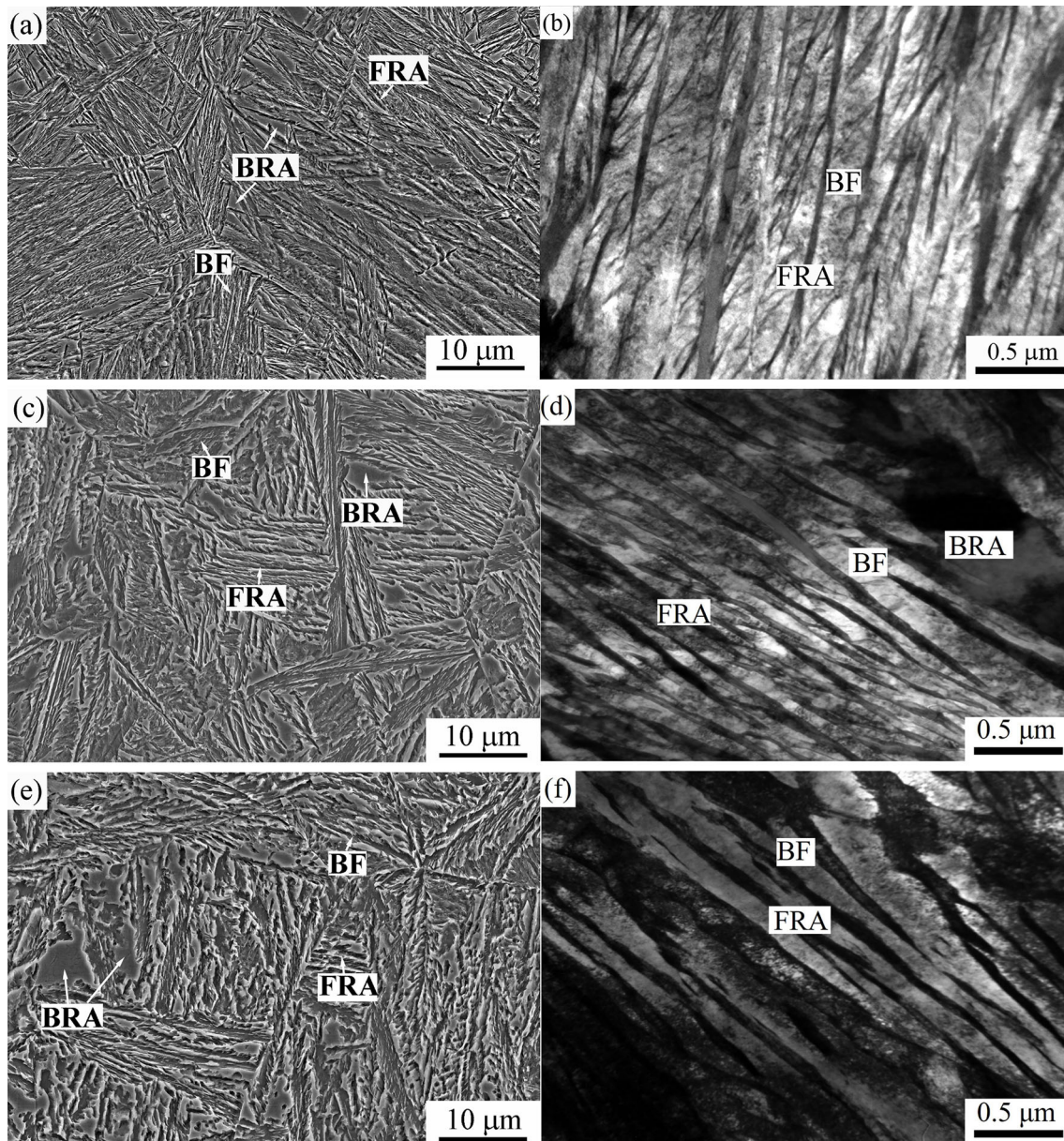


Fig. 2 SEM (a, c, e) and TEM (b, d, f) microstructures in studied steel after austempering at 270 °C (a, b), 350 °C (c, d) and 370 °C (e, f)

Table 1 Parameters of microstructure features for studied steel

Austempering temperature/°C	Holding time/h	$V_{RA}/\%$	$C_{RA}/wt.\%$	$V_{BRA}/\%$	t_{FRA}/nm	t_{BF}/nm	$L_{BF}/\mu m$
270	2	7.39	1.28	2.1 ± 0.5	40 ± 2.3	76 ± 3.4	15 ± 0.4
350	2	17.26	0.83	3.5 ± 0.5	96 ± 6.5	120 ± 5.1	22 ± 1.3
370	2	15.87	0.88	4.2 ± 1.2	75 ± 5.6	122 ± 4.5	21 ± 0.6

$$\bar{L}_T^{BF} = \pi t_{BF}/2 \quad (8)$$

According to Table 1, the sample subjected to austempering at 350 °C has the highest volume fraction of RA, the

lowest carbon content in RA, and the largest film-like RA. The transformation driving force of bainite reduces with the decrease in austempering temperature from 350 to 270 °C. Hence, the volume fraction of RA increases firstly.

However, the obtained RA in the sample subjected to austempering at 370 °C decreases. This result is likely caused by the increase in diffusion carbon coefficient at 370 °C. This increase results in the rapid diffusion of carbon in the new BF product into the neighboring RA. Thus, the ferrite plate grows to epitaxy and swallows up a part of RA, consequently decreasing the volume fraction of RA at 370 °C. The sizes of BF plates and bainite sheaves increase with austempering temperature. They almost peak at 350 °C.

The size distributions of bainitic ferrite plate thickness, bainite sheaf length, and film-like retained austenite thickness are presented in Fig. 3 for further analysis of microstructural features. The size distribution of bainite sheaves, BF plate, and film-like RA changes from small to large with the increase in austempering temperatures. Compared with the sample treated at 270 °C, the samples treated at 350 and 370 °C exhibit a more uniform size distribution and larger scale and scope. As inferred from

Fig. 3, the thickness distribution of the film-like RA in the sample subjected to austempering at 270 °C is mainly limited within 20–40 nm, whereas the size distribution in the sample subjected to austempering at 370 °C is limited within 40–80 nm. However, in the sample subjected to austempering at 350 °C, the size of RA film is more uniformly distributed and dispersed.

In solid transformation, crystal anisotropy will strongly affect the local structure of phase interfaces. Figure 4 shows the orientation imaging of the whole microstructure (left) and bainitic ferrite misorientation distribution maps (right) of the samples subjected to austempering at 270, 350, and 370 °C. When the austempering temperature is 270 °C, the misorientation distribution of bainite sheaves is predominantly marked by a substantial 50°–60° misorientation angle, aligning with the microstructural feature of lower bainite [43]. When the austempering temperature is 350 °C, the proportion of the misorientation angle < 20° corresponding to the microstructure feature of upper

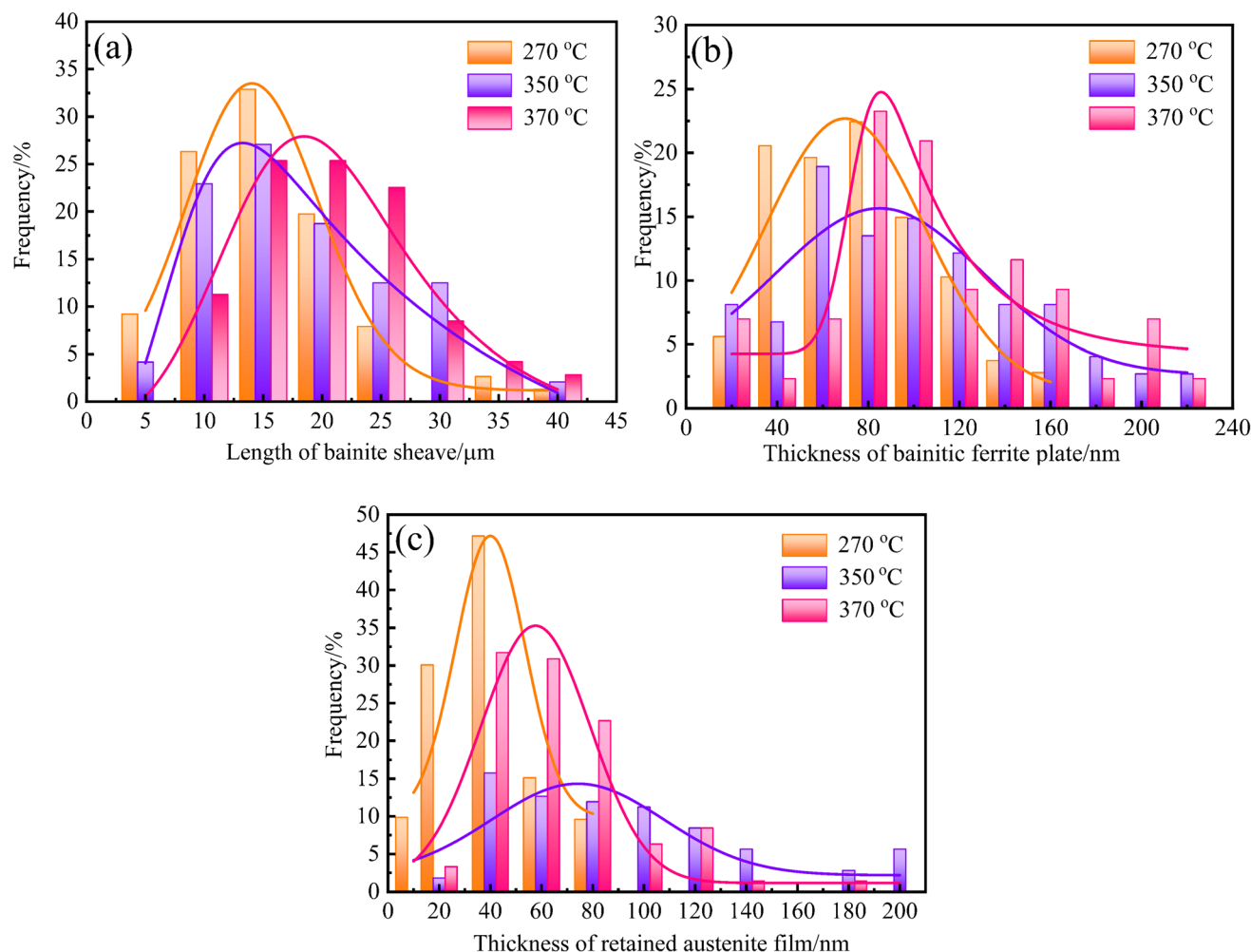


Fig. 3 Distribution of microstructure size in studied steel after austempering at various temperatures. **a** Bainite sheaf length; **b** thickness of BF plate; **c** thickness of film-like RA

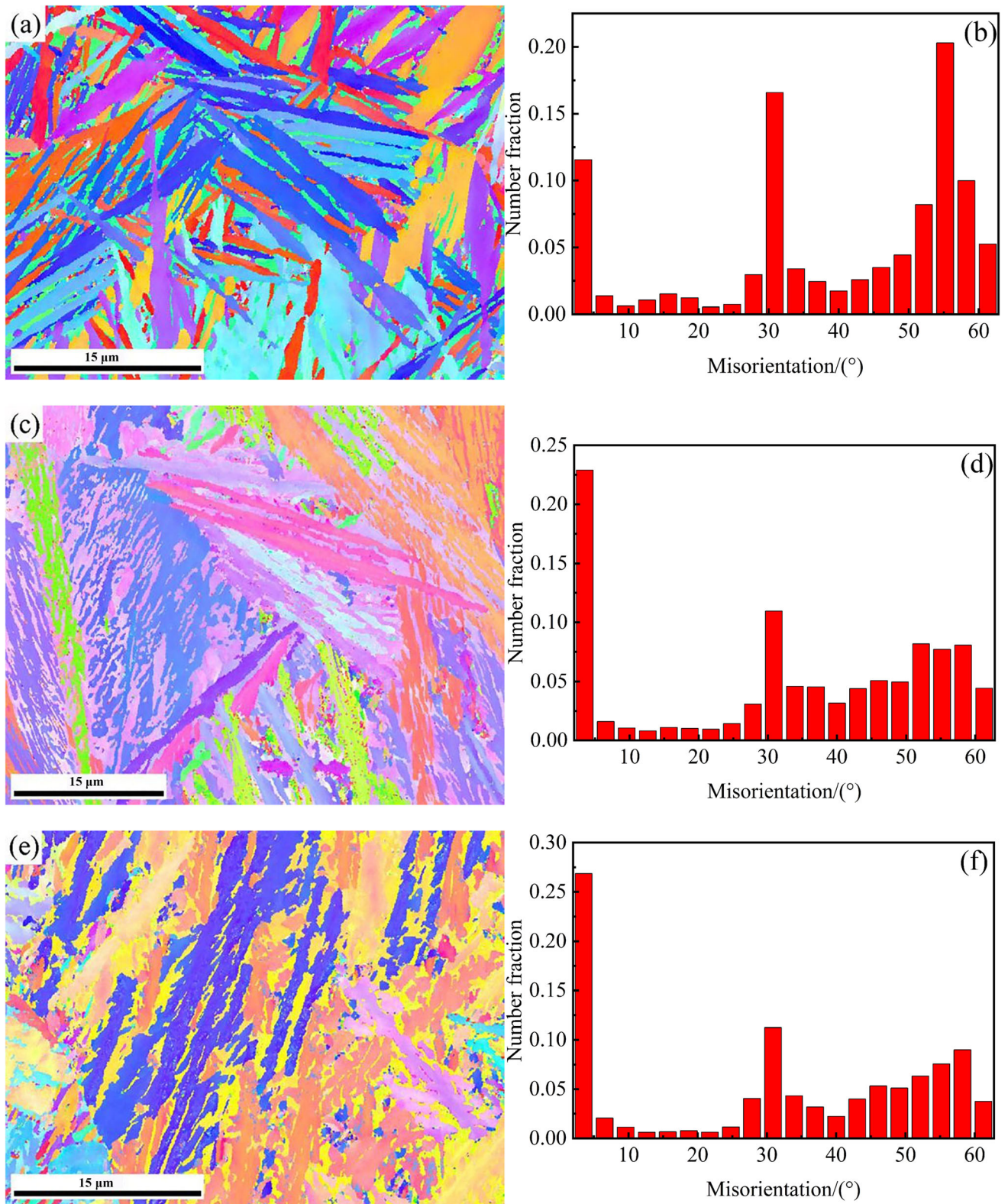


Fig. 4 Orientation image (a, c, e) and misorientation angle distribution (b, d, f) in studied samples after austempering at 270 °C (a, b), 350 °C (c, d), and 370 °C (e, f)

Table 2 Ultimate tensile strength (UTS), yield strength (YS), total elongation (TE), uniform elongation (δ_{UE}), impact toughness (α_{KU}), and work-hardening exponent (e) of studied steel

Austempering temperature/°C	Holding time/h	UTS/MPa	YS/MPa	TE/%	$\delta_{UE}/\%$	$\alpha_{KU}/(\text{J cm}^{-2})$	e
270	2	1860	1147	14.5	6.9	64.9	0.14
350	2	1555	931	19.2	15.6	60.6	0.19
370	2	1520	1027	20.1	18.1	45.1	0.16

bainite is large [43]. When the temperature is further increased to 370 °C, the misorientation angle distribution of the sample becomes similar to that of the sample treated at 350 °C.

4.2 Mechanical properties

Table 2 shows the mechanical properties of the studied steels. As the temperature for bainite transformation is increased, ultimate tensile strength and impact toughness decrease, whereas total elongation and uniform elongation increase. The sample subjected to austempering at 350 °C has the lowest yield strength and highest work-hardening exponent. The sample subjected to austempering at 270 °C possesses high ultimate strength and yield strength but low elongation. Figure 5 presents the engineering stress versus engineering strain curves and true stress vs. true strain curves of the studied steel. The samples subjected to austempering at 270 °C exhibit apparent necking phenomenon. By contrast, uniform deformation dominates deformation behavior in the samples subjected to austempering at temperatures above 350 °C. The sample hence displays a slow strain hardening state and nearly has no necking.

4.3 Tensile simulation results

Figure 2 clearly illustrates that all austempering microstructures contain blocky and film-like RA. To explore the impact of different retained austenite morphologies on tensile deformation behavior, finite element simulations were conducted using SEM microstructure obtained at 350 °C austempering as a representative example, as depicted in Fig. 6a and c. It is well understood that unstable blocky RA is susceptible to phase transformation-induced plasticity (TRIP) transformation into martensite during actual deformation. Therefore, this study initially assumes that BRA has transformed into martensite in the simulation, while the FRA remains unchanged due to its high mechanical stability. Following a series of image processing steps, a two-dimensional RVE model of the microstructure region was acquired, as shown in Fig. 6b and d. The martensite–bainitic ferrite microstructure model

is referred to as M-BF and the film-like retained austenite and bainitic ferrite model is referred to as FRA-BF. Subsequently, RVE model was imported into ANSYS finite element software, and two-dimensional plane strain elements were utilized for mesh generation. To accurately capture the geometric deformation of materials in micro-mechanical modeling, boundary conditions for RVE were defined. Specifically, a displacement load was applied to the right side of RVE to permit unrestricted movement in the horizontal direction, while a fixed constraint was imposed on the left boundary. By dividing the displacement by the original length of RVE, the engineering strain in the horizontal direction could be precisely calculated.

The flow curves of each phase were computed according to Eq. (3) as depicted in Fig. 7. The yield strength of martensite is approximately three times that of bainitic ferrite, suggesting that deformation in M-BF model will primarily be accommodated by bainitic ferrite. In FRA-BF model, the flow stresses of film-like retained austenite and bainitic ferrite gradually tend to converge with increasing flow strain.

The tensile test simulation of a two-dimensional RVE model based on real microstructure was conducted at a strain rate of $4 \times 10^{-3} \text{ s}^{-1}$, with the loading direction indicated by the red arrow. Figures 8 and 9 depict the distribution of equivalent plastic strain and von Mises stress in RVE models across various engineering strains, respectively. In M-BF model, martensite exhibits minimal strain. The strain is primarily confined to BF at a 45° angle relative to the tensile direction. Furthermore, the strain failure zone can be seen in BF. As the engineering strain increases, von Mises stress disperses from the martensite interface to the bainite phase. Conversely, FRA-BF model exhibits excellent plastic deformation coordination. The strain is uniformly distributed between BF and RA without any noticeable localization. With the increase in engineering strain, the von Mises stress between the retained austenite and bainitic ferrite gradually intensifies, and yet there is no apparent stress concentration.

As shown in Fig. 8d, h, at a total engineering strain of 10%, the average equivalent plastic strain values of BF phase in M-BF and FRA phase in FRA-BF model are 1.5 and 0.9 times the total strain value, respectively. Moreover,

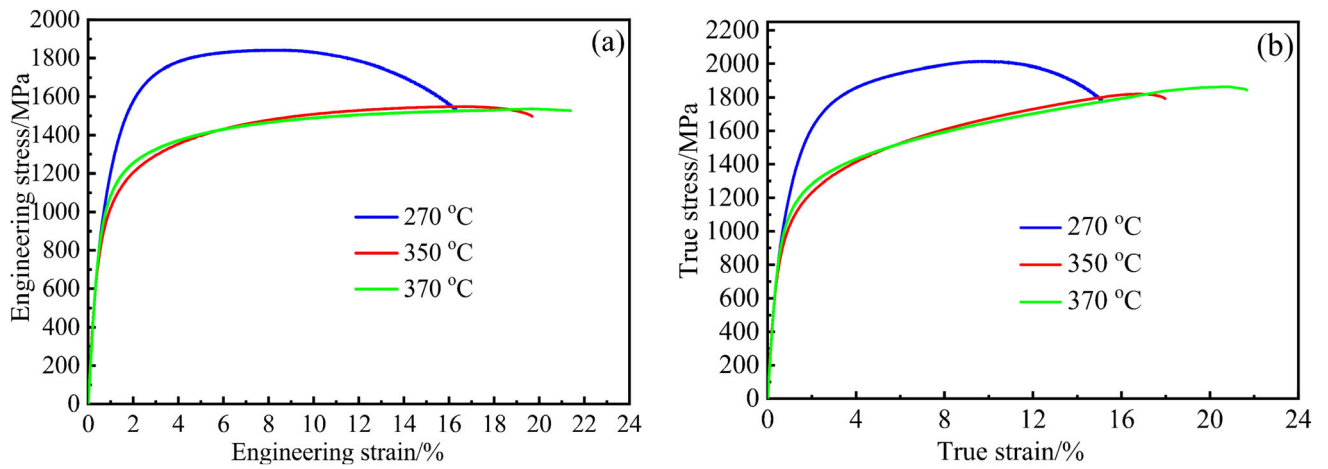


Fig. 5 Engineering stress versus engineering strain curves (a) and true stress versus true strain curves (b) of studied steel

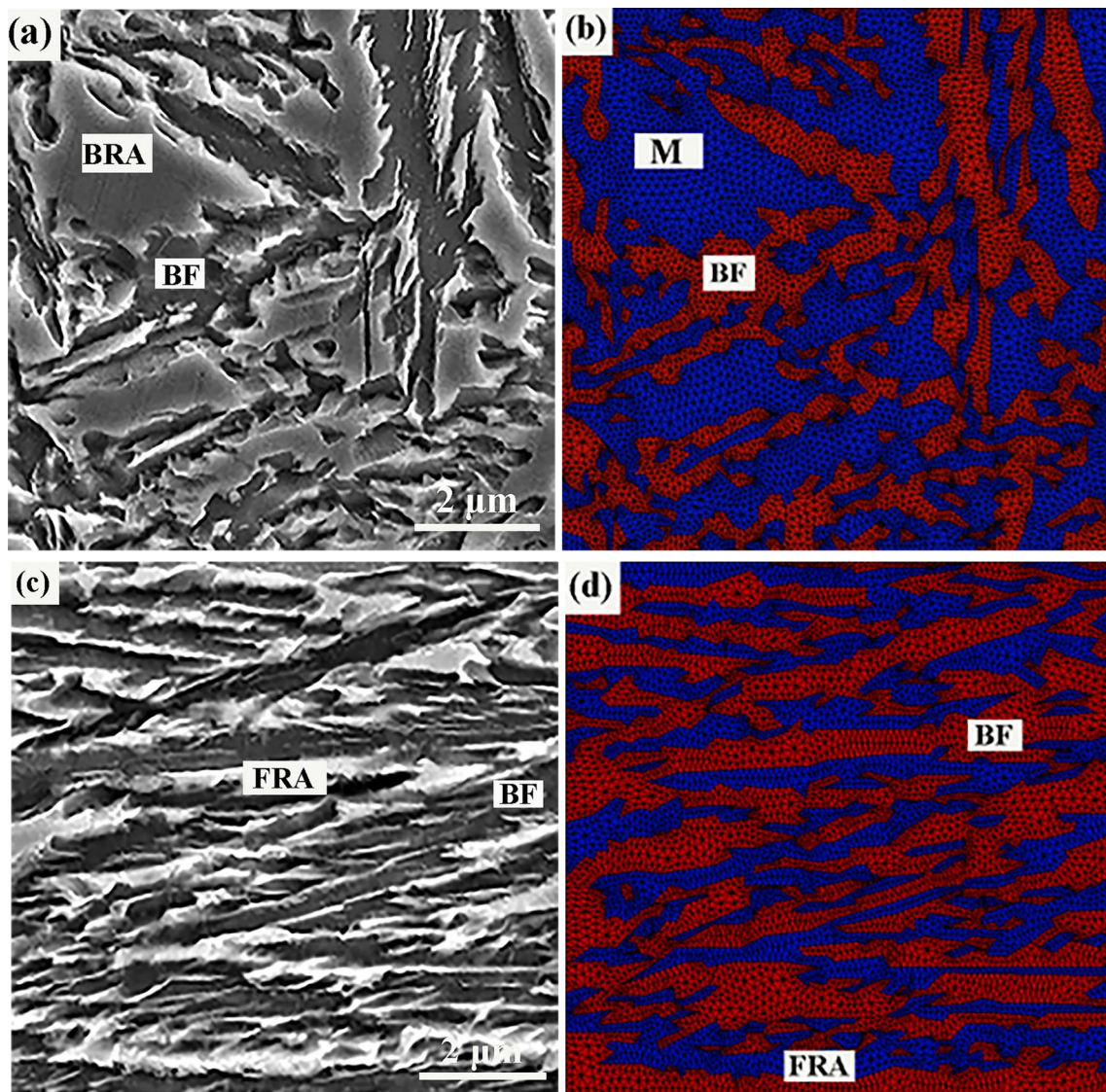


Fig. 6 SEM microstructure obtained at austempering at 350 °C (a, c) and their corresponding RVE models (b, d). a, b M-BF model; c, d FRA-BF model

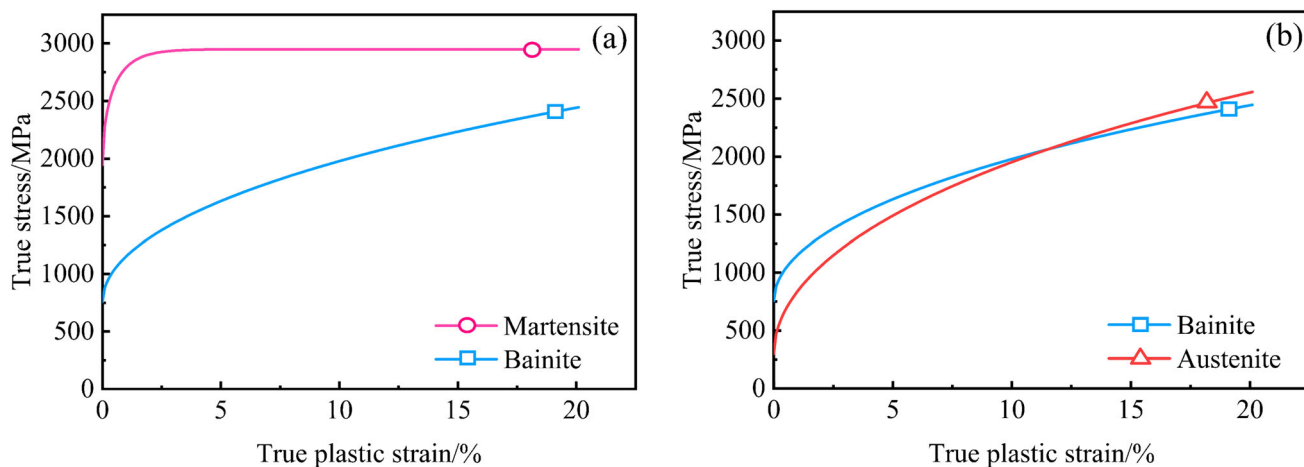


Fig. 7 Flow curves of each phase in sample subjected to austempering at 350 °C. **a** M-BF; **b** FRA-BF

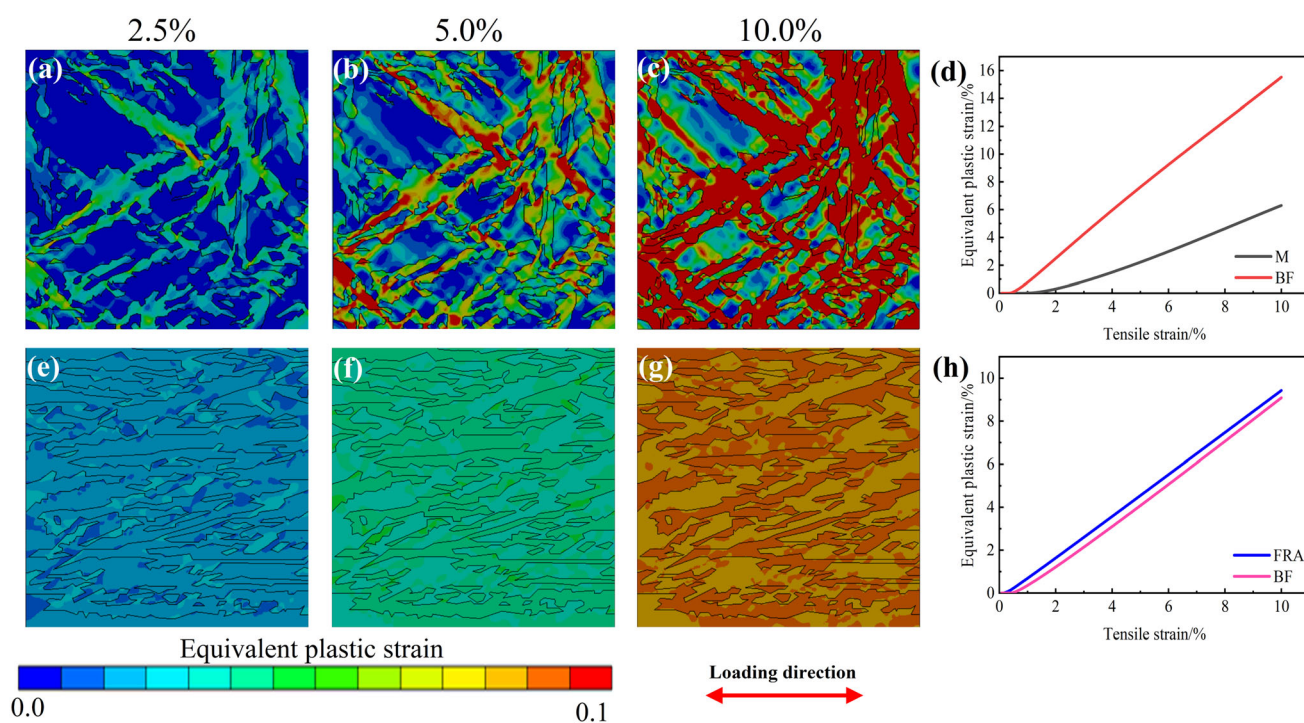


Fig. 8 Equivalent plastic strain distribution of M-BF model (**a–d**) and FRA-BF model (**e–h**) and their corresponding evolution curves (**d, h**) with total tensile strains

at some high-strain locations, these values can reach approximately 2–5 times the total strain. In M-BF model, this phenomenon is attributed to the gradual concentration of von Mises stress, ultimately leading to nonuniform deformation and the localization of equivalent plastic strain within the area. As the strain increases to 10%, the high-strain concentration areas in BF are interconnected in a

direction approximately 45° to the loading direction, forming mutually perpendicular strain failure bands. In contrast, in FRA-BF model, there is no apparent von Mises stress concentration phenomenon in the thin FRA and BF, resulting in a uniform distribution of equivalent plastic strain between the two phases. And there is no strain failure zone even at the total engineering strain of 10%.

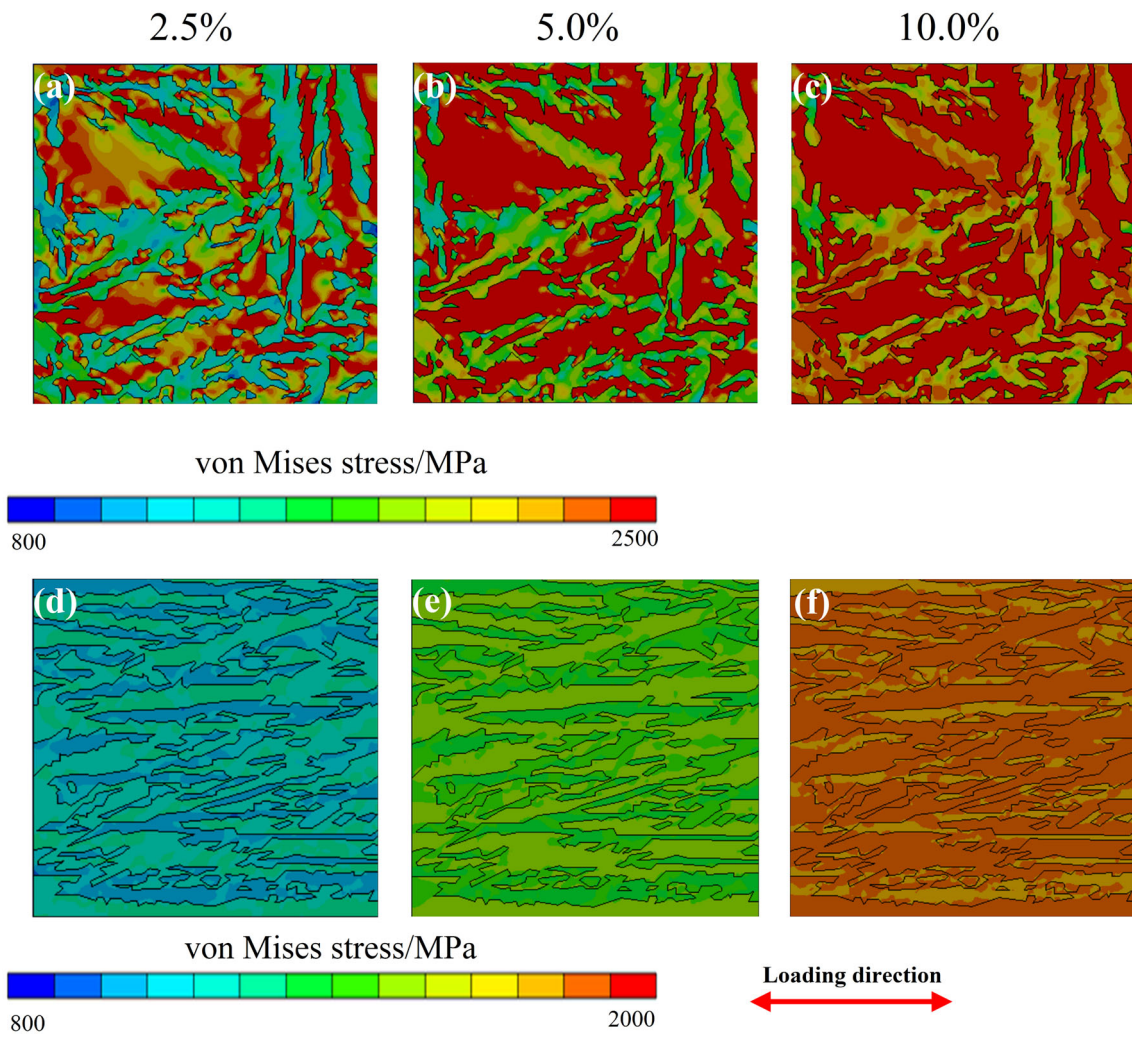


Fig. 9 Von Mises stress distribution of M-BF model (a–c) and FRA-BF model (d–f) under different total tensile strains

5 Discussion

5.1 Correlation between microstructure and mechanical property

The comprehensive properties of the studied steel subjected to different austempering temperatures are compared as shown in the radar plots in Fig. 10. The sample subjected to austempering at 270 °C possesses the best combination of strength and toughness with the loss of plasticity. The sample treated at 350 °C has the best combination of plasticity and toughness at the cost of strength. The sample presents good plasticity performance only when the austempering temperature is further increased to 370 °C.

The sizes of laths and bainite sheaves in the bainite are crucial for strengthening [44–46] and toughening [47, 48]. Strength is a function of lath and bainite sheaf dimensions, which is expressed as [49]:

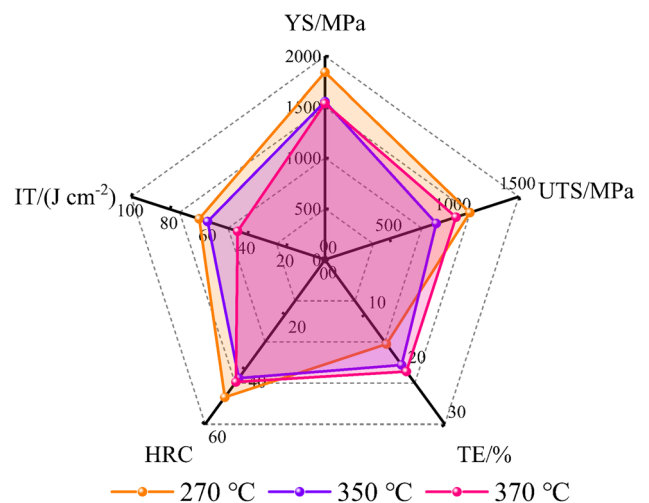


Fig. 10 Radar plots representing comprehensive properties of studied steel after different austempering treatments. IT—Impact toughness; HRC—Rockwell hardness

$$\sigma = (\sigma_e + \sigma_{SS} + \sigma_{cem}) + k^m M^{-1} \quad (9)$$

where σ_e is a lattice friction stress term; σ_{SS} arises from the solid solution strengthening effect; σ_{cem} is the carbide dispersion strengthening term; k is analogous to the Hall–Petch parameter; and M is a geometrical parameter related to the average slip band length to the size of bainite sheaf and ferrite lath.

$$M = 2/\pi \left\{ t_{BF} \ln \tan \left(\frac{\arccos \left(\frac{t_{BF}}{L_{BF}} \right) + \frac{\pi}{4}}{2} \right) + \frac{\pi}{2L_{BF}} - L_{BF} \arccos \left(\frac{t_{BF}}{L_{BF}} \right) \right\} \quad (10)$$

According to the data in Table 1, M values of the samples subjected to austempering at 270, 350, and 370 °C treatments can be calculated to be 0.34, 0.78, and 0.79, respectively. In this case, σ_e and σ_{SS} are approximately the same. σ_{cem} is equal to zero because carbide does not exist in this case. Therefore, according to Eq. (9), an inverse linear relationship exists between yield stress and M value. The calculated M value increases when the austempering temperature is increased from 270 to 350 °C. This behavior corresponds to the decrease in yield strength in concordance with the experimental results. The size of bainite microstructures is associated with crystal anisotropy at different austempering temperatures. Local variants form during bainite transformation to adjust the strain caused by the transformation from austenite to bainite [50]. The upper bainite subjected to austempering at 350 and 370 °C exhibits coarse bainite sheaves due to few variable selections [51]. When the austempering temperature is decreased to 270 °C, the driving force and self-adjustment of strain increase [50]. Thus, the selection of variants increases, and the angle between bainite sheaves with various variants enlarges; this effect eventually results in increasing the proportion of mismatch angles at 50°–60° and reducing the size of bainite sheaves. Moreover, fine bainite sheaves with various crystallographic orientations can further increase the toughness of nanostructured bainitic steels by causing consecutive changes in the crack growth direction [52]. The high proportion of large misorientation angles between fine bainite sheaves in the sample treated at 270 °C can cause crack branching and inhibit crack propagation, thus further increasing toughness.

Works by some researchers [9–11] suggest that 350 °C is the optimal temperature for stabilizing retained austenite and achieving the best performance match at that temperature. However, in this work, when compared to samples austempered at 270 and 370 °C, the sample treated at 350 °C exhibits the lowest yield strength. The values of t_{BF} , L_{BF} , and M for the samples subjected to austempering at 350 and 370 °C are almost similar, indicating that the

difference in yield strength between the two samples is not caused by the ferrite structure. After austempering at 350 °C, the sample exhibits the highest volume fraction of retained austenite, the lowest carbon content in retained austenite, and larger sizes of film-like retained austenite, all contributing to the reduction in yield strength. However, due to the more dispersed size distribution of film-like retained austenite with a larger span, it can continuously induce strain-induced martensite transformation during tensile deformation [53, 54]. In conjunction with the relatively larger bainitic ferrite plate size, this results in the highest work-hardening index, ultimately leading to higher ultimate strength, improved total elongation, and uniform elongation. Under austempering at 370 °C, the diffusion coefficient of carbon increases, enabling rapid diffusion into the surrounding retained austenite following the formation of bainitic ferrite. This process causes the plates to extend outward and engulf some of the retained austenite, thereby slightly reducing the volume of retained austenite and slightly increasing the carbon content in the retained austenite. Additionally, the smaller size of film-like retained austenite in the sample subjected to austempering at 370 °C also contributes to the increase in yield strength.

When the austempering temperatures are 350 and 370 °C, the size of bainitic ferrite plate and bainite sheaf remains similar. Hence, the quantity, morphology, size, and stability of retained austenite are important factors in defining the toughness of the steel [9–11, 33, 52, 55]. As shown in Table 1, the retained austenite percentage of the sample after austempering at 350 °C is marginally higher than that of the sample after austempering at 370 °C; however, the sample austempered at 350 °C exhibits less blocky retained austenite, indicating a higher proportion of film-like retained austenite. Due to its smaller size and increased carbon content, film-like retained austenite can generally withstand stress more steadily, enhancing the material toughness by suppressing the propagation of cracks through crack deflection and closure mechanisms [45, 52]. In contrast, blocky retained austenite, with its larger size, is more susceptible to transforming into hard and brittle martensite under external forces, thereby acting as initiation points for crack formation and consequently diminishing toughness [56, 57]. In this study, the carbon content in the retained austenite following austempering at 350 °C is lower, and its overall stability is inferior to that achieved at 370 °C. Nonetheless, the sample subjected to austempering at 350 °C demonstrates superior impact toughness. Therefore, the primary factor contributing to the enhanced impact toughness of the samples austempered at higher temperatures in this work is the volume fraction of film-like retained austenite.

5.2 Correlation between microstructure and strain partitioning

The study by Stanford et al. [58] suggests that strain localization can be minimized when the strength of the hard phase is not much different from that of the soft phase. In the tensile deformation process of M-BF model (Fig. 8), the ratio of σ_{BF}/σ_M is discerned to be approximately 3 (Fig. 7a), with BF phase emerging as the principal bearer of strain. This leads to a pronounced localization of strain within BF phase, particularly under conditions of high strain, as graphically represented in Fig. 8d. In FRA-BF model, the ratio of σ_{FRA}/σ_{BF} approaches 1 (Fig. 7b), indicating the minimizing strain localization as shown in Fig. 8e–g. A comparison of strain ratios between the two models during deformation is performed, as depicted in Fig. 11. When the tensile strain is less than 3%, $\varepsilon_{FRA}/\varepsilon_{BF}$ is much lower than $\varepsilon_{BF}/\varepsilon_M$. Although the difference in strain ratios between the two models becomes small with the increase in the total tensile strain, the strain ratio of $\varepsilon_{FRA}/\varepsilon_{BF}$ is always lower than that of $\varepsilon_{BF}/\varepsilon_M$. This suggests a more uniform distribution of strain between FRA and BF, along with improved coordination during deformation. The localization degree of stress distribution in FRA-BF model is also lower compared to that in M-BF model, as evident from the Von Mises stress results (Fig. 9). It can be attributed to the higher strength and enhanced resistance to slip exhibited by FRA. The small size of FRA confirms the available space for deformation, preventing BF from mitigating its stress by inducing deformation in FRA, and thereby expediting its transition into a plastic deformation state. Additionally, BF present in FRA-BF model may possess a higher density of dislocations and an increased number of dislocation sources, facilitating its quicker transition into the plastic deformation state, consistent with

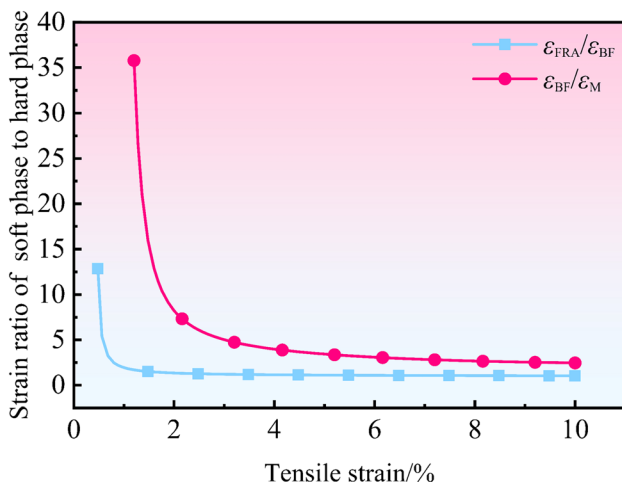


Fig. 11 Evolution of strain ratio between soft phase and hard phase with total tensile strain

the experimental results reported by Hojo et al. [59]. Consequently, this results in a slightly lower strain ratio in FRA model. The excellent coordination of plastic deformation between FRA and BF can make the sample have good plasticity. In contrast, BF region in M-BF model exhibits pronounced strain concentration. The presence of the hard phase, martensite, introduces plastic incompatibility, resulting in notable strain gradients at interfaces, which could lead to dislocation accumulation. This accumulation, in turn, causes stress concentration, acting as the initiation site for cracks during tensile deformation, and ultimately deteriorating the performance of the material [60, 61]. This aligns with the experimental and simulation findings conducted by Hajizad et al. [62], where initially in the simulation, unstable RA fully converts into martensite, thereby making BF the primary strain bearer. Localized strain primarily accumulates in the narrow channel between martensite and bainite [38, 57], leading to the initiation of damage. Subsequently, cracks propagate along the interface of BF/M. Microstructural examinations near the tensile fracture surfaces in Fig. 12 demonstrate that microcracks initiate and propagate at the interface between M/BRA and BF. More crack observations can be seen in the Supplementary Materials. This observation indicates that the stress-induced BRA to martensite transformation in the early deformation stage may improve the strength to a certain extent, but it is harmful to the subsequent plastic coordinated deformation.

6 Conclusions

1. The sample subjected to low-temperature austempering exhibits the optimal combination of strength and toughness while sacrificing plasticity. Conversely, the sample subjected to intermediate-temperature austempering demonstrates superior plasticity and toughness at the expense of strength.
2. With increasing austempering temperature, the size distribution of bainite sheaves, BF plates, and film-like RA transitions from smaller to larger dimensions. Fine BF plates and bainite sheaves tend to enhance both strength and toughness. Moreover, the broad angle misorientation distribution within bainite sheaves contributes to the reduction in the size of these microstructures.
3. The broad distribution in size and shape of RA achieved through intermediate-temperature austempering is advantageous for preserving work-hardening capacity, thereby enhancing overall plasticity and uniform plasticity. In this context, the volume fraction of the ductile film-like retained austenite within the microstructure assumes a pivotal role in improving

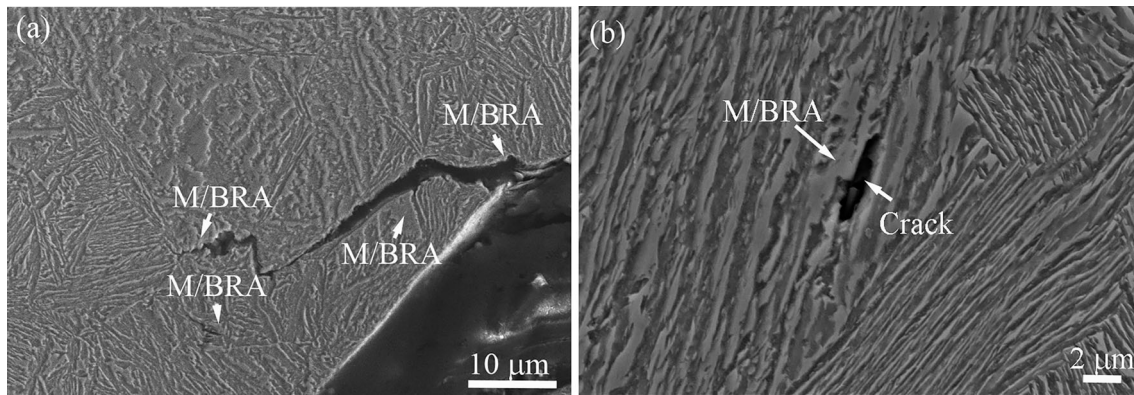


Fig. 12 Crack initiated and propagated along M/BRA near tensile fracture surfaces. **a** Relatively long crack; **b** microcrack

impact toughness under relatively higher austempering temperatures.

- In the uniaxial tension RVE simulations, stress primarily concentrates in the hard phase. In M-BF model, BF phase acts as the primary phase for localized plastic strain accumulation. As strain accumulates, localized strain concentration zones emerge in the microstructure oriented at a 45° angle to the loading direction. Microcrack will initiate along with the boundary between martensite and bainitic ferrite, which is verified by the experimental result. In contrast, a uniform distribution of plastic strain is obtained between the film-like retained austenite and bainitic ferrite in FRA-BF model, which will enhance the plastic deformation coordination and the total plasticity.

Supplementary Information The online version contains supplementary material available at <https://doi.org/10.1007/s42243-024-01310-6>.

Acknowledgements This work was supported by the National Key R&D Program Young Scientists Project (2021YFB3703500), National Natural Science Foundation of China (52001110, 52122410, 52374406), S&T Program of Hebei (23311004D), Natural Science Foundation of Hebei Province (E2023203259), and Science and Technology Project of Yantai (2022ZDCX002).

Declarations

Conflict of interest The authors declare that they have no known competing financial interests or personal relationships that could have appeared to influence the work reported in this paper.

References

- X. Long, R. Zhang, F. Zhang, G. Du, X. Zhao, *Mater. Sci. Eng. A* 760 (2019) 158–164.
- J.F.M. Vergnol, J.R. Grilhe, *J. Phys. France* 45 (1984) 1479–1490.
- C. Garcia-Mateo, F.G. Caballero, H.K.D.H. Bhadeshia, *ISIJ Int.* 43 (2003) 1238–1243.
- F.G. Caballero, H.K.D.H. Bhadeshia, *Curr. Opin. Solid State Mater. Sci.* 8 (2004) 251–257.
- X.Y. Long, F.C. Zhang, J. Kang, B. Lv, X.B. Shi, *Mater. Sci. Eng. A* 594 (2014) 344–351.
- H.K.D.H. Bhadeshia, D.V. Edmonds, *Met. Sci.* 17 (1983) 411–419.
- J.A. da Cruz, T.F.M. Rodrigues, V.D.C. Viana, D.B. Santos, *MSF* 706–709 (2012) 173–180.
- B. Avishan, S. Yazdani, S. Hossein Nedjad, *Mater. Sci. Eng. A* 548 (2012) 106–111.
- A. Misra, S. Sharma, S. Sangal, A. Upadhyaya, K. Mondal, *Mater. Sci. Eng. A* 558 (2012) 725–729.
- A. Varshney, S. Sangal, S. Kundu, K. Mondal, *Mater. Des.* 95 (2016) 75–88.
- J. Zhao, B. Lv, F. Zhang, Z. Yang, L. Qian, C. Chen, X. Long, *Mater. Sci. Eng. A* 742 (2019) 179–189.
- S. Khare, K. Lee, H.K.D.H. Bhadeshia, *Metall. Mater. Trans. A* 41 (2010) 922–928.
- B. Berisha, C. Raemy, C. Becker, M. Gorji, P. Hora, *Acta Mater.* 100 (2015) 191–201.
- A. Ramazani, M. Abbasi, S. Kazemiabnavi, S. Schmauder, R. Larson, U. Prahl, *Mater. Sci. Eng. A* 660 (2016) 181–194.
- J. Kadkhodapour, S. Schmauder, D. Raabe, S. Ziaei-Rad, U. Weber, M. Calcagnotto, *Acta Mater.* 59 (2011) 4387–4394.
- A. Das, S. Tarafder, S. Sivaprasad, D. Chakrabarti, *Mater. Sci. Eng. A* 754 (2019) 348–360.
- J.H. Kim, D. Kim, F. Barlat, M.G. Lee, *Mater. Sci. Eng. A* 539 (2012) 259–270.
- A. Ch. Darabi, H.R. Chamani, J. Kadkhodapour, A.P. Anaraki, A. Alaie, M.R. Ayatollahi, *Mech. Mater.* 110 (2017) 68–83.
- J. Ha, J. Lee, J.H. Kim, M.G. Lee, F. Barlat, *Int. J. Plast.* 93 (2017) 89–111.
- K.S. Choi, W.N. Liu, X. Sun, M.A. Khaleel, *Acta Mater.* 57 (2009) 2592–2604.
- X. Sun, K.S. Choi, A. Soulami, W.N. Liu, M.A. Khaleel, *Mater. Sci. Eng. A* 526 (2009) 140–149.
- K.S. Choi, W.N. Liu, X. Sun, M.A. Khaleel, *Metall. Mater. Trans. A* 40 (2009) 796–809.
- N. Fujita, N. Ishikawa, F. Roters, C.C. Tasan, D. Raabe, *Int. J. Plast.* 104 (2018) 39–53.
- Z. Zhao, M. Ramesh, D. Raabe, A.M. Cuitiño, R. Radovitzky, *Int. J. Plast.* 24 (2008) 2278–2297.
- S.H. Choi, E.Y. Kim, W. Woo, S.H. Han, J.H. Kwak, *Int. J. Plast.* 45 (2013) 85–102.
- H. Monshat, S. Serajzadeh, *Ironmak. Steelmak.* 46 (2019) 513–521.

- [27] W.S. Owen, M. Grujicic, *Acta Mater.* 47 (1998) 111–126.
- [28] M. Nygåards, P. Gudmundson, *Comput. Mater. Sci.* 24 (2002) 513–519.
- [29] G. Moeini, A. Ramazani, V. Sundararaghavan, C. Koenke, *Mater. Sci. Eng. A* 689 (2017) 89–95.
- [30] H. Vafaenezhad, A. Yazdi, S.H. Seyedein, M.R. Aboutalebi, A.R. Eivani, F. Hosseinabadi, *Mater. Sci. Eng. A* 799 (2021) 140131.
- [31] B. Cullity, S. Stock, *Elements of X-ray diffraction*, 3rd ed., Prentice-Hall, New York, USA, 2001.
- [32] C.F. Jaczak, *Retained austenite and its measurement by X-ray diffraction*, SAE Technical Paper, 1980, pp. 800426.
- [33] C. Hofer, F. Winkelhofer, H. Clemens, S. Primig, *Mater. Sci. Eng. A* 664 (2016) 236–246.
- [34] D. De Knijf, C. Föjer, L.A.I. Kestens, R. Petrov, *Mater. Sci. Eng. A* 638 (2015) 219–227.
- [35] G.I. Rees, H.K.D.H. Bhadeshia, *Mater. Sci. Technol.* 8 (1992) 994–1003.
- [36] M. Zhang, X. Yang, J. Kang, F. Zhang, Z. Yang, *Materials* 13 (2020) 4703.
- [37] R.M. Rodriguez, I. Gutiérrez, *Mater. Sci. Forum* 426–432 (2003) 4525–4530.
- [38] A. Kumar, A. Dutta, S.K. Makineni, M. Herbig, R.H. Petrov, J. Sietsma, *Mater. Sci. Eng. A* 757 (2019) 107–116.
- [39] J. Bouquerel, K. Verbeke, B. Decoeman, *Acta Mater.* 54 (2006) 1443–1456.
- [40] A. Ramazani, K. Mukherjee, U. Pohl, W. Bleck, *Metall. Mater. Trans. A* 43 (2012) 3850–3869.
- [41] A. Ramazani, K. Mukherjee, A. Abdurakhmanov, U. Pohl, M. Schleser, U. Reisgen, W. Bleck, *Mater. Sci. Eng. A* 589 (2014) 1–14.
- [42] G. Béres, Z. Weltsch, *Periodica Polytechnica Transportation Engineering* 47 (2018) 206–212.
- [43] S. Zajac, V. Schwinn, K.H. Tacke, *Mater. Sci. Forum* 500–501 (2005) 387–394.
- [44] K. Zhu, O. Bouaziz, C. Oberbillig, M. Huang, *Mater. Sci. Eng. A* 527 (2010) 6614–6619.
- [45] X.Y. Long, J. Kang, B. Lv, F.C. Zhang, *Mater. Des.* 64 (2014) 237–245.
- [46] C. García-Mateo, F.G. Caballero, H.K.D.H. Bhadeshia, *Mater. Sci. Forum* 500–501 (2005) 495–502.
- [47] L. Rancel, M. Gómez, S.F. Medina, I. Gutierrez, *Mater. Sci. Eng. A* 530 (2011) 21–27.
- [48] F.G. Caballero, H.K.D.H. Bhadeshia, K.J.A. Mawella, D.G. Jones, P. Brown, *Mater. Sci. Technol.* 18 (2002) 279–284.
- [49] D.V. Edmonds, R.C. Cochrane, *Metall. Trans. A* 21 (1990) 1527–1540.
- [50] T. Furuhashi, H. Kawata, S. Morito, G. Miyamoto, T. Maki, *Metall. Mater. Trans. A* 39 (2008) 1003–1013.
- [51] T. Furuhashi, H. Kawata, S. Morito, T. Maki, *Mater. Sci. Eng. A* 431 (2006) 228–236.
- [52] A. Kumar, A. Singh, *Mater. Sci. Eng. A* 729 (2018) 439–443.
- [53] A. Varshney, S. Sangal, S. Kundu, K. Mondal, *Mater. Des.* 99 (2016) 439–448.
- [54] Y.X. Qiao, Z.B. Zheng, H.K. Yang, J. Long, P.X. Han, *Iron Steel Res. Int.* 30 (2023) 1463–1476.
- [55] C. Leng, H. Yang, G. Yi, H. Lo, J. Li, Y. Li, *Mater. Werkstofftech.* 55 (2024) 7–12.
- [56] S.I. Lee, J.M. Lee, S.G. Kim, Y.B. Song, H.K. Kim, J.H. Shim, B. Hwang, *Mater. Sci. Eng. A* 848 (2022) 143334.
- [57] S.B. Zhou, C.Y. Hu, F. Hu, L. Cheng, O. Isayev, S. Yershov, H.J. Xiang, K.M. Wu, *Mater. Sci. Eng. A* 846 (2022) 143175.
- [58] N. Stanford, J. Wang, T. Hilditch, *Int. J. Fatigue* 129 (2019) 105218.
- [59] T. Hojo, M. Koyama, B. Kumai, Y. Shibayama, A. Shiro, T. Shobu, H. Saitoh, S. Ajito, E. Akiyama, *Scripta Mater.* 210 (2022) 114463.
- [60] M. Calcagnotto, Y. Adachi, D. Ponge, D. Raabe, *Acta Mater.* 59 (2011) 658–670.
- [61] T. Wang, L. Qian, K. Li, F. Zhang, J. Meng, *Mater. Sci. Eng. A* 819 (2021) 141498.
- [62] O. Hajizad, A. Kumar, R.H. Petrov, J. Sietsma, R. Dollevoet, Z. Li, *Comput. Mater. Sci.* 202 (2022) 110965.

Springer Nature or its licensor (e.g. a society or other partner) holds exclusive rights to this article under a publishing agreement with the author(s) or other rightsholder(s); author self-archiving of the accepted manuscript version of this article is solely governed by the terms of such publishing agreement and applicable law.